IOPscience iopscience.iop.org

Home Search Collections Journals About Contact us My IOPscience

Enhancing Tomo-PIV reconstruction quality by reducing ghost particles

This article has been downloaded from IOPscience. Please scroll down to see the full text article.

2013 Meas. Sci. Technol. 24 024010

(http://iopscience.iop.org/0957-0233/24/2/024010)

View the table of contents for this issue, or go to the journal homepage for more

Download details:
IP Address: 128.250.248.173
The article was downloaded on 02/01/2013 at 05:00

Please note that terms and conditions apply.

Meas. Sci. Technol. **24** (2013) 024010 (11pp) doi:10.1088/0957-0233/24/2/024010

Enhancing Tomo-PIV reconstruction quality by reducing ghost particles

C M de Silva, R Baidya and I Marusic

Department of Mechanical Engineering, The University of Melbourne, Victoria 3010, Australia

E-mail: c.desilva3@pgrad.unimelb.edu.au

Received 29 March 2012, in final form 23 May 2012
Published 20 December 2012
Online at stacks.iop.org/MST/24/024010

Abstract
A technique to enhance the reconstruction quality and consequently the accuracy of the velocity vector field obtained in Tomo-PIV experiments is presented here. The methodology involves detecting and eliminating spurious outliers in the reconstructed intensity field (ghost particles). A simulacrum matching-based reconstruction enhancement (SMRE) technique is proposed, which utilizes the characteristic shape and size of actual particles to remove ghost particles in the reconstructed intensity field. An assessment of SMRE is performed by a quantitative comparison of Tomo-PIV simulation results and DNS data, together with a comparison to Tomo-PIV experimental data measured in a turbulent channel flow at a matched Reynolds number ($Re_\tau = 937$) to the DNS study. For the simulation data, a comparative study is performed on the reconstruction quality based on an ideal reconstruction determined from known particle positions. The results suggest that a significant improvement in the reconstruction quality and flow statistics is achievable at typical seeding densities used in Tomo-PIV experiments. This improvement is further amplified at higher seeding densities, enabling the use of up to twice the typical seeding densities currently used in Tomo-PIV experiments. A reduction of spurious vectors present in the velocity field is also observed based on a median outlier detection criterion. The application of SMRE to Tomo-PIV experimental data shows an improvement in flow statistics, comparable to the improvement seen in simulations. Finally, due to the non-iterative nature of SMRE, the increase in processing time is marginal since only a single pass of the reconstruction algorithm is required.

Keywords: Tomo-PIV, ghost particles, reconstruction quality, wall turbulence

(Some figures may appear in colour only in the online journal)

1. Introduction

Three-dimensional, three-component (3D–3C) velocity measurement techniques have become increasingly available over the past decade, particularly in the area of particle image velocimetry. These techniques include holographic PIV (HPIV) (Barnhart *et al* 1994), 3D scanning PIV (Brücker 1996), defocusing PIV (Willert and Gharib 1992), 3D particle tracking velocimetry (PTV) (Maas *et al* 1993), synthetic aperture PIV (SAPIV) (Belden *et al* 2010) and tomographic-PIV (Tomo-PIV) (Elsinga *et al* 2006).

This paper focuses on Tomo-PIV, which is based on a volumetric reconstruction of an intensity field that is imaged from multiple views. Tomo-PIV has several advantages over other 3D–3C PIV techniques mentioned previously. For example, it overcomes issues in HPIV such as a single line of sight, complex experimental setups and high seeding densities which lead to speckle noise (Adrian 2005). Techniques such as PTV are limited to low seeding densities yielding low spatial resolution in comparison to Tomo-PIV (Worth and Nickels 2008). Furthermore, scanning PIV is limited to applications where the laser-sheet scanning rates exceed the fastest flow time scales. The main drawbacks of Tomo-PIV include the requirement of a very accurate calibration procedure and the high sensitivity to reconstruction quality. In addition, this technique is also hindered by a relatively high computational cost caused by the reconstruction procedure and the three-dimensional cross-correlation involved in post-processing. However, Tomo-PIV has been extensively used for the analysis

 © 2013 IOP Publishing Ltd Printed in the UK & the USA

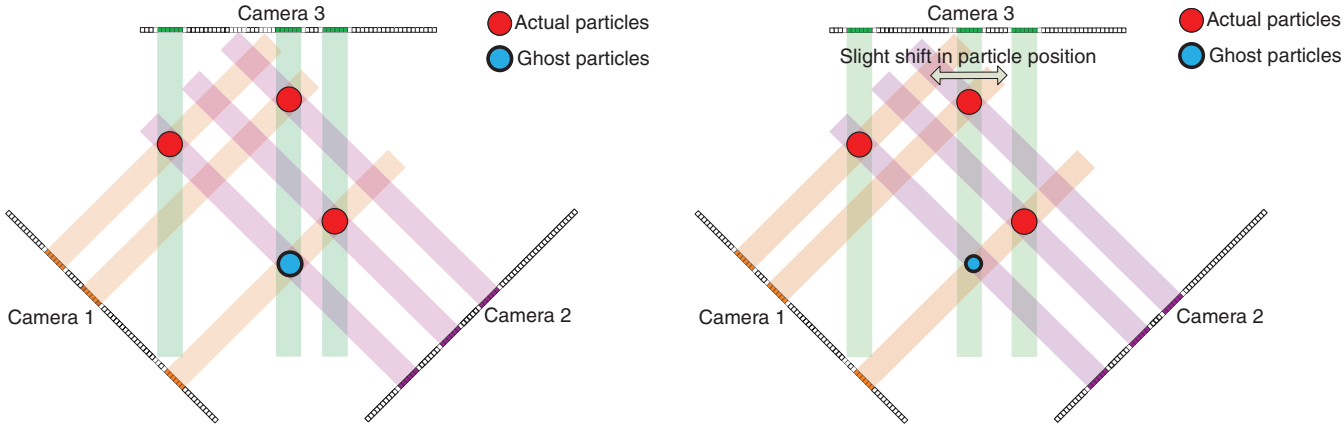

(*a*) Ideal overlap from all three cameras (*b*) Typical scenario observed in a reconstructed volume

Figure 1. (*a*) Formation of ghost particles in a three-camera projection, which take a similar shape to an actual particle (a rare scenario). (*b*) Formation of a typical ghost particle in a three-camera projection, which has an irregular shape, depending on the overlap between projections of the actual particles present (a frequently occurring scenario).

of turbulent flows in studies performed by Scarano and Poelma (2009), Schröder *et al* (2008), Atkinson *et al* (2011) and Scarano *et al* (2006) to name a few.

1.1. Ghost particles

In a typical Tomo-PIV experiment, a reconstruction is performed to produce a volumetric three-dimensional intensity field from two-dimensional images. Unlike other applications of tomography, such as in medical applications where a large knowledge of the reconstructed volume is available via several projections, Tomo-PIV is generally limited to three to six projections. This lack of projection information leads to a non-unique solution to the algebraic reconstruction, which in turn leads to the formation of ghost particles where the lines of sight of multiple particles intersect from several projections as illustrated in figure 1(*a*). They appear as spurious intensity peaks in the reconstructed intensity field together with the actual particles. Consequently, ghost particles introduce errors to the cross-correlation, particularly for high seeding densities (Elsinga *et al* 2006).

This study proposes a technique to isolate ghost particles based on their shape and size compared to actual particles in the reconstructed intensity field. Typically, in a reconstructed intensity field, actual particles have a predominant spherical shape and mean size. Since Tomo-PIV is run at lower seeding densities than planar PIV, particles combining together in the intensity field is not as common. This enables us to distinguish the majority of the particles individually within the reconstructed intensity field. In addition, due to overlap between lines of sight between particles (figure 1), which is commonly present in the reconstructed intensity field, ghost particles tend to consist of irregular shapes that are predominantly smaller than actual particles depending on the camera configuration. This is shown in a simplified schematic in figure 1 using a three-camera configuration. Figure 1(*a*) shows an ideal scenario where the overlap of the three projections causes the ghost particle to have the same shape and intensity as an actual particle. However, as shown in figure 1(*b*), a slight deviation in particle positions results in a variation of the ghost particle's shape. Figure 2 shows this variation in particle shape in a typical reconstructed intensity field.

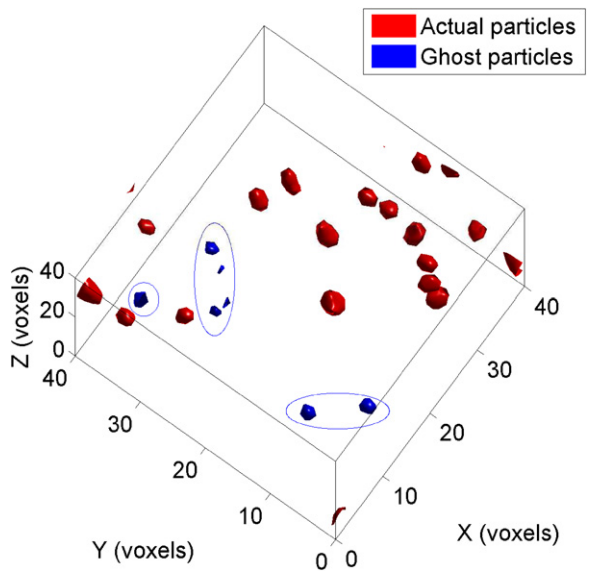

Figure 2. A volumetric region from a reconstructed intensity field of $40 \times 40 \times 40$ voxels showing the consistency in the shape of actual particles versus the predominantly smaller and irregular shapes of ghost particles which are encapsulated by ⬭.

In the following sections, the working principles of SMRE are described. The performance of SMRE is assessed using Tomo-PIV simulations by a quantitative comparison between reconstructions performed with and without SMRE. An assessment on real Tomo-PIV data is performed using a data set obtained from a channel flow experiment by a comparison of flow statistics against direct numerical simulations (DNS) at a matched Reynolds number.

Throughout this paper, we use the coordinate system x, y and z to refer to the streamwise, spanwise and wall-normal directions with corresponding velocity components given by U, V and W. The superscript + refers to normalization with the viscous inner scale. For example, $l^+ = lU_\tau/\nu$ and

$U^+ = U/U_\tau$, where U_τ is the friction velocity and ν is the kinematic viscosity of the fluid.

2. SMRE algorithm

The technique utilizes a template-matching scheme based on calculating the sum of squared differences (SSD block matching) that is expressed as

$$\Gamma(x_T, y_T, z_T) = \sum_{x,y,z} [E(x, y, z) - T(x - x_T, y - y_T, z - z_T)]^2, \quad (1)$$

where E is the reconstructed intensity field (volume) and the summation is over x, y, z in the region containing the feature T (template) positioned at x_T, y_T, z_T. The template in equation (1) consists of a uniform intensity equal to the mean background intensity level and has a size of $T_{sz} \times T_{sz} \times T_{sz}$ voxels. It should be noted that the mean background intensity level is typically close to zero depending on the noise present in the reconstructed intensity field. A detailed numerical assessment is performed on the size of the template (T_{sz}), which is one of the main parameters of the proposed algorithm. The volume E in equation (1) includes the whole reconstructed intensity field, therefore Γ is calculated across E. Once Γ is determined, a histogram-based thresholding technique is then applied. The thresholding eliminates any outliers that exist in areas where the image quality is poor, such as when reflections are present from a surface. This minimizes the effect of spurious intensity values in determining the infinity norm of Γ ($|\Gamma|_\infty$), which is used in

$$\Gamma(x_T, y_T, z_T)_{\text{norm}} = \frac{\Gamma(x_T, y_T, z_T)}{|\Gamma(x_T, y_T, z_T)|_\infty}, \quad (2)$$

to normalize Γ to the range 0 to 1. Γ_{norm} provides a map to determine voxels that are suspected to be ghost particles or background where Γ_{norm} is close to zero. This is caused by ghost particles being predominantly smaller than actual particles, which leads to a low Γ_{norm}. Conversely, a high value of Γ_{norm} close to 1 indicates the presence of actual particles. An additional benefit of the technique is that it also eliminates irregularities or noise present in the intensity field due to small foreign objects such as dust. These objects are known to cause a bias in the cross-correlation phase in the surrounding region if present (Scarano and Poelma 2009). To perform the elimination process, a threshold for Γ_{norm} (Γ_{th}) is determined to nullify voxels where $\Gamma_{\text{norm}} < \Gamma_{\text{th}}$. The selection of an optimal Γ_{th} is discussed with greater detail in section 3.2.2.

Since we use a block-matching technique, the magnitude of Γ_{norm} can vary based on the intensity level of voxels for a given shape of particles. However, the magnitude of Γ_{norm} is primarily determined by the shape of particles present in the reconstructed intensity field. In addition, algorithms for reconstruction, such as MLOS-SMART (Atkinson and Soria 2009), result in ghost particles typically having a lower intensity level than actual particles. Therefore, the reliance on the intensity level should assist the elimination process. It should be noted that this technique fails to detect ghost particles that are larger in size with similar intensity values to the actual particles, since this results in a high Γ_{norm}. However, this also prevents nullifying actual particles that show up coalesced to form large particles in the reconstructed intensity field. A rigorous analysis on the accuracy of positive detections is discussed in section 3.1.

SMRE is a non-iterative process, and thus requires only a single pass of the reconstruction procedure. Considering the computationally intensive nature of the reconstruction procedure, this is a considerable advantage in terms of overall processing time, compared to other iterative ghost reduction techniques (Novara *et al* 2010).

3. Assessment of SMRE

A detailed assessment on the performance of SMRE is done using a simulation study which utilizes synthetic Tomo-PIV images. The simulations involve three main components: a calibration process, a reconstruction and a three-dimensional cross-correlation. A detailed description of the methodology of the simulations is provided by de Silva *et al* (2012). It should be noted that the same algorithms are used for processing both the simulation data and the experimental results presented in section 4. The simulations use a DNS velocity field at $Re_\tau = 934$ (del Alamo *et al* 2004) to displace the particles. The use of DNS data provides a realistic flow field compared to using a simplified flow field such as a constant displacement (Lecordier and Westerweel 2008). In addition, the simulations include a Phong lighting reflection model (Phong 1975), which is used to obtain a near Gaussian light intensity distribution on the spherical particles. This is then refined using a 'Mie scatter' model, which is an improved representation of the light scattered by particles in PIV experiments. The cameras are modelled in three-dimensional space with lens distortion effects and camera noise which is added to the synthetic images. In our study, the images consist of two-dimensional projections from a three-dimensional object. In comparison, most studies utilize a two-dimensional object projected onto a one-dimensional synthetic image (Elsinga *et al* 2006, Novara *et al* 2010).

Each simulation performed provides the three velocity components U, V, W within the reconstructed volume. From this information, we are able to determine flow statistics within the reconstructed volume. These statistics are then determined from the DNS data at the same interrogation volume positions. This ensures that a relative comparison is made between the Tomo-PIV technique and the DNS data (de Silva *et al* 2012).

A summary of the parameters used in the simulations is given in table 1. A four-camera setup is used with the cameras placed on a single side of the laser sheet as illustrated in figure 3. The cameras are positioned within the optimal angles as specified by de Silva *et al* (2012) for the given configuration to obtain the maximum achievable reconstruction quality. For the analysis performed, only a four-camera setup is considered, as this is the most commonly used in practice. We did not consider using three or fewer cameras as preliminary results suggested that the particle shapes are not defined well. This hinders the ability to distinguish between ghost and actual particles. In addition, more than four projections are typically not used as it increases the cost and complexity of the

Table 1. Summary of parameters used in the simulation study.

Number of cameras	4
Dynamic range of each camera	8 bit
Laser-sheet thickness	$\approx 0.1\delta$
Synthetic noise level	10% of maximum intensity
Particle size (Mie scatter model)	$\approx$1–4 μm
Wavelength of light (Mie scatter model)	532 μm
Flow medium (Mie scatter model)	Air
Mean particle diameter	3 voxels
Voxel size (l_v^+)	≈ 0.6
Reconstruction volume size	$\approx 1\delta \times 1\delta \times 0.1\delta$, where δ corresponds to the half channel height
Reconstruction volume size (voxels)	$1500 \times 1500 \times 150$
z^+ position of reconstructed volume	$\approx 50 < z^+ < 150$
Number of velocity vectors	$\approx 180 \times 180 \times 15$
Velocity field overlap	$75\% \times 75\% \times 75\%$
Interrogation volume length (l^+)	≈ 20
Interrogation volume size (voxels)	$32 \times 32 \times 32$
Reconstruction algorithm	MLOS-based in-house technique (de Silva *et al* 2012) which uses a third-order polynomial calibration fit and a bi-cubic interpolation scheme to determine the voxel intensities to sub-pixel accuracy.
Cross-correlation algorithm	Template-matching scheme based on Lewis (1995) which incorporates several advancements discussed by Scarano (2001).

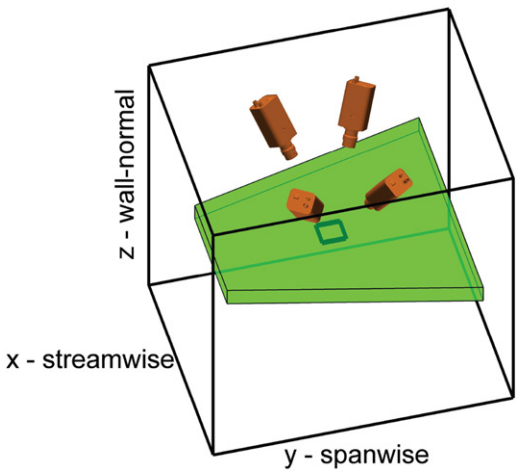

Figure 3. All cameras placed on a single side of the laser.

tomographic system without a substantial benefit (Elsinga *et al* 2006). An interrogation volume length of 20 inner viscous units ($l^+ = 20$) in x, y and z directions is used for the cross-correlation as by de Silva *et al* (2012). The seeding particle movement is approximately 25% of the interrogation volume length, which satisfies the quarter voxel displacement criterion suggested by Keane and Adrian (1992). In addition, the voxel to pixel size ratio in all simulations is approximately equal to 1 as suggested by Elsinga *et al* (2006).

3.1. Reconstruction quality

To assess the effect of SMRE on the reconstruction quality, we use the quality factor (Q), which is determined using

$$Q = \frac{\sum_{x,y,z} E_1(x,y,z) \cdot E_0(x,y,z)}{\sqrt{\sum_{x,y,z} E_1^2(x,y,z) \cdot \sum_{x,y,z} E_0^2(x,y,z)}}, \quad (3)$$

where $E_1(x,y,z)$ is the reconstructed intensity field, and $E_0(x,y,z)$ is an ideal reconstruction intensity field based on known particle positions (Elsinga *et al* 2006). An improvement in the reconstruction quality is indicated by an increase in Q towards 1, and it depends primarily on the number of projections available and the seeding density. A quantitative analysis of Q enables us to determine any effect that the technique has on actual particles, since the elimination of actual particles will cause a reduction in Q. Therefore, an improvement in Q indicates a reduction in ghost particles with minimal impact on the actual particles present in the intensity field. It should be noted that an increase in Q should result in an improved accuracy of the velocity field which is the primary purpose of using SMRE.

Figure 4 shows the reconstruction quality before and after the application of SMRE at various seeding densities N_s (Adrian and Westerweel 2011). As discussed in sections 3.2.1 and 3.2.2, the optimum T_{sz} and Γ_{th} are used at each N_s for the simulations in this comparison. The results suggest a clear improvement in Q at all N_s, particularly at higher N_s. This is expected as these cases are more prone to ghost particles due to an increase in the overlap between projections of actual particles. This trend is also observed by Novara *et al* (2010) using the MTE-MART algorithm to reduce ghost particles where the effectiveness is higher when N_s increases. It should be noted that values obtained for Q are lower than those observed by Elsinga *et al* (2006) using two-dimensional simulations. This is expected as the simulations in this analysis use a three-dimensional reconstruction, which results in a fundamental reduction in the reconstruction quality Q as demonstrated by Elsinga *et al* (2006). A quantitative analysis on this variation is discussed in detail by de Silva *et al* (2012).

Figure 4(*b*) show an improvement of over 20% in Q in the range $0.17 < N_s < 0.35$, which encapsulates the seeding densities used in most Tomo-PIV experiments. The improvement observed in Q then drops above $N_s > 0.35$, which is caused by the poor reconstruction quality attainable at these seeding densities, which makes these cases irrecoverable.

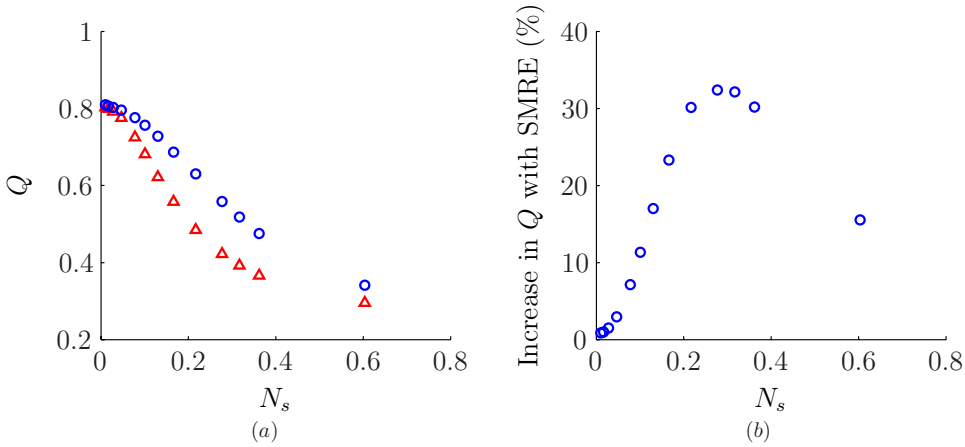

Figure 4. (*a*) Reconstruction quality factor (Q) obtained prior to (△) and after (○) the use of SMRE as a function of N_s. (*b*) Percentage improvement in Q at each N_s.

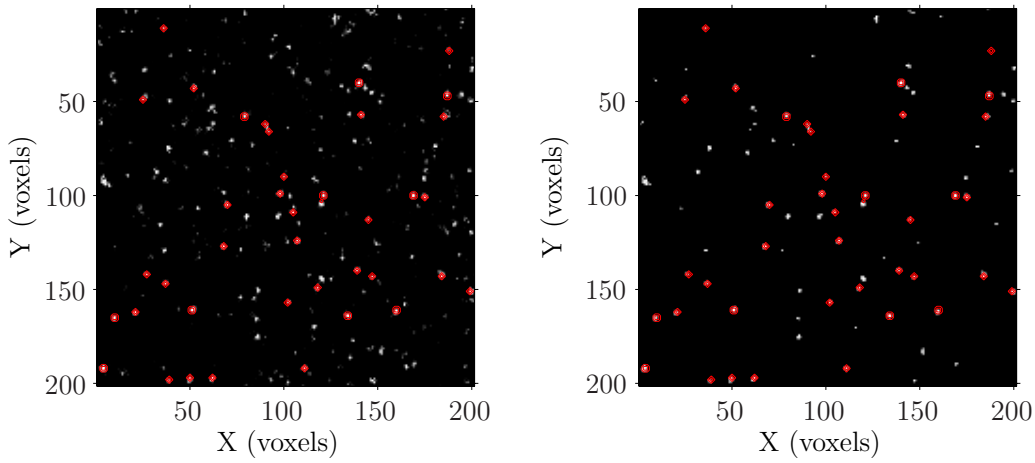

(*a*) Unmodified streamwise-spanwise plane from a reconstructed intensity field.

(*b*) Modified streamwise-spanwise plane from a reconstructed intensity field using SMRE.

Figure 5. A comparison of a streamwise–spanwise plane (200 × 200 voxels) from a reconstructed intensity field prior to and after the use of SMRE. The red contours indicate actual particles from an ideal reconstruction based on known particle positions. The simulation considered has an improvement of 30% in Q after modifying the reconstructed intensity field.

Figures 5(*a*) and (*b*) show a streamwise–spanwise plane of a three-dimensional intensity field, where the actual particles are indicated by red contours. A clear reduction in ghost particles can be seen in figure 5(*b*) compared with figure 5(*a*), which is an unmodified reconstruction intensity field. Figure 5(*b*) shows that the majority of the actual particles have a similar shape and the technique has minimal impact on these particles. It should be noted that the change in particle size observed in figure 5 is caused by a variation in the intersection between the particles relative to the streamwise–spanwise plane location. Furthermore, we can see that the remaining ghost particles present in figure 5(*b*) have a predominantly similar shape to actual particles, and therefore remain undetected by SMRE.

Figure 6 shows the influence of the laser-sheet thickness (Δ_L). The improvement in Q reduces as the laser-sheet thickness is increased beyond 0.1δ; we believe this is due to the error associated with reconstructing a thicker volume with a limited number of projections. Conversely, using a thin laser-sheet thickness below 0.1δ causes the number of ghost particles to decrease, therefore the impact of SMRE is reduced leading to a lower improvement in Q.

Figure 7 shows an analysis of the number of spurious vectors present in the simulations at various N_s based on a median test detection criterion suggested by Westerweel and Scarano (2005). The results suggest an improvement of approximately 20% after the application of SMRE at seeding densities typically used in Tomo-PIV experiments. A larger improvement is seen at higher seeding densities as the reconstruction quality is poor prior to the application of SMRE in this regime. Furthermore, similar to the results obtained for Q a high percentage of spurious vectors are observed for $N_s > 0.35$ due to the poor reconstruction quality. Nevertheless, an improvement is still achieved after the application of SMRE.

3.2. Optimum parameters

3.2.1. Selection of an optimal T_{sz}. The seeding density (N_s) is known to significantly impact the reconstruction quality (Elsinga *et al* 2006). In this section, we analyse the influence that N_s has on the selection of the template size (T_{sz}), which

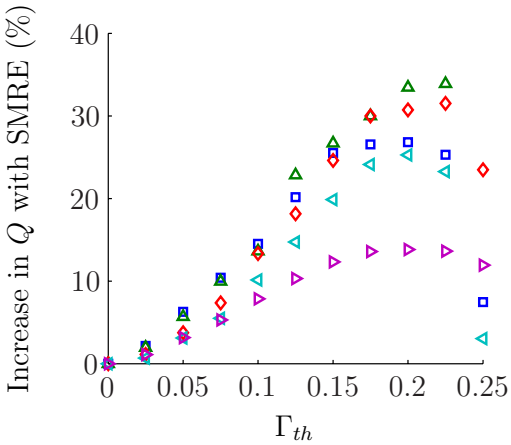

Figure 6. Improvement in the reconstruction quality Q obtained at varying laser-sheet thicknesses (Δ_L) and Γ_{th}. The symbols □, △, ◇, ◁ and ▷ correspond to $\Delta_L = 0.05\delta$, 0.10δ, 0.15δ, 0.20δ and 0.25δ respectively.

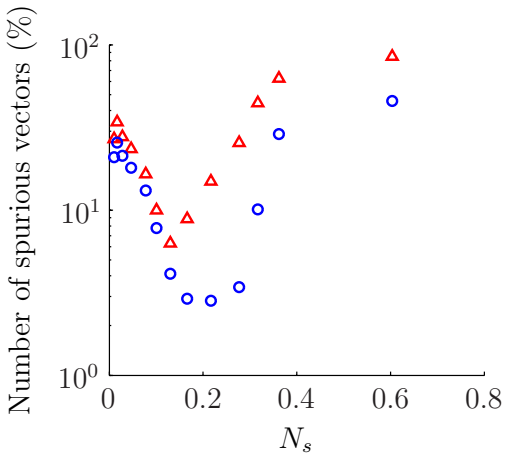

Figure 7. Percentage of spurious vectors detected in the velocity field with (○) and without (△) the application of SMRE based on the detection criteria suggested by Westerweel and Scarano (2005).

is one of the main parameters of SMRE. Simulations are run at several T_{sz} and N_s while maintaining the other parameters constant as given in table 1. To determine the accuracy of each simulation a comparison is made between flow statistics of the simulation and the DNS data as described earlier. Therefore, it should be noted that the result presented from this comparison is directly applicable for wall-bounded turbulent flows with large wall-normal heterogeneity. However, we believe that it provides a qualitative indication of the optimum parameters for other flows. This comparison is made between simulation and DNS statistics averaged over the same interrogation volume length used in the simulations (averaged DNS statistics). The averaged DNS statistics are obtained by applying a three-dimensional mean box filter on the DNS fields obtained from del Alamo *et al* (2004). Figure 8(*a*) shows the accuracy of the mean streamwise velocity $\langle U\rangle^+$ for varying N_s and T_{sz}. The angular brackets denote volumetric averaging across the reconstructed volume in the range $50 < z^+ < 150$. Similarly, figure 8(*b*) shows the accuracy of the kinetic energy $\langle k\rangle^+$ for the fluctuations of the velocity components. $\langle k\rangle^+$ is defined as

$$\langle k\rangle^+ = \tfrac{1}{2}[\langle u^2\rangle^+ + \langle v^2\rangle^+ + \langle w^2\rangle^+], \tag{4}$$

where u, v and w are the fluctuations of the streamwise, spanwise and wall-normal velocity components, respectively. This enables a quantitative analysis on the accuracy for all three fluctuations of the velocity components rather than analysing them individually. To ensure the trend of the accuracy shown by $\langle k\rangle^+$ is consistent with the second-order statistics of the three velocity components, a comparison is also made between them as shown in figure 9. Since the overall trend observed is similar, we use $\langle k\rangle^+$ to quantify the accuracy of second-order statistics throughout this paper. In addition, the optimal Γ_{th} is used at all N_s considered. This is determined using equation (5) as described in section 3.2.2. The range considered in the analysis for seeding density includes the typical range used for Tomo-PIV experiments ($0.15 < N_s < 0.25$). It should be noted that at lower seeding densities ($N_s < 0.15$), the accuracy drops due to insufficient particles to obtain a good cross-correlation peak, while at higher seeding densities ($N_s > 0.35$), the accuracy

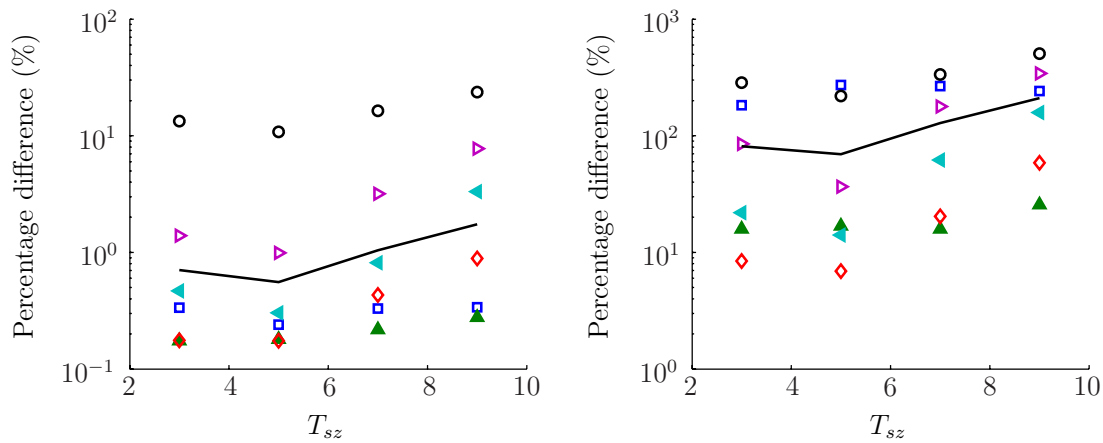

(*a*) Accuracy of $\langle U\rangle^+$. (*b*) Accuracy of $\langle k\rangle^+$.

Figure 8. Comparison of simulation and averaged DNS statistics at varying T_{sz} and N_s with a mean particle diameter of three voxels. The symbols □, ▲, ◇, ◀, ▷ and ○ correspond to $N_s = 0.13$, 0.16, 0.22, 0.27, 0.31 and 0.36 respectively. The solid line shows the trend of the error. Statistics are obtained by means of a volumetric average across the reconstructed volume in the range $50 < z^+ < 150$.

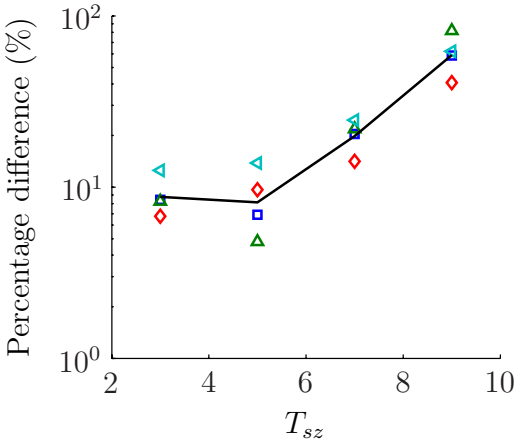

Figure 9. Comparison of simulation results and averaged DNS statistics for $\langle u^2\rangle^+$ (△), $\langle v^2\rangle^+$ (◇), $\langle w^2\rangle^+$ (◁) and $\langle k\rangle^+$ (□) in the range $50 < z^+ < 150$ at varying T_{sz} with a $N_s = 0.22$ and a mean particle diameter of three voxels. The solid line shows the trend of the error.

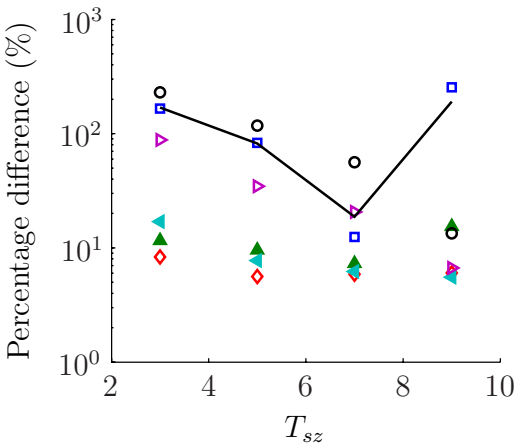

Figure 10. Comparison of simulation results and averaged DNS statistics for $\langle k\rangle^+$ in the range $50 < z^+ < 150$ at varying T_{sz} and N_s with a mean particle diameter of five voxels. The symbols □, ▲, ◇, ◀, ▷ and ○ correspond to $N_s = 0.13, 0.16, 0.22, 0.27, 0.31$ and 0.36 respectively. The solid line shows the trend of the error.

drops due to the poor reconstruction quality (Elsinga *et al* 2006).

Figure 8 shows that the optimal T_{sz} (five voxels) is independent of the seeding density as indicated by the error trend line in figures 8(*a*) and (*b*). This is expected as the detection algorithm is based on shape and size. Similarly, the parameter T_{sz} is independent of the laser-sheet thickness.

The simulations performed thus far are at a mean particle diameter of three voxels. Figure 10 shows the effect of increasing the mean particle diameter to five voxels. This is achieved by increasing the voxel discretization level while maintaining the same physical particle size, which should increase the overall accuracy. The results indicate that the optimum T_{sz} increases proportionally to the mean particle diameter observed in the reconstructed intensity field. This is expected as the technique is based on distinguishing ghost particles based on shape and the proportion of the template occupied by the particles present in the reconstructed intensity field. The results indicate that T_{sz} should be ideally 1–2 voxels larger than the mean particle diameter. Thereafter, we observe that the accuracy drops off when T_{sz} is larger than 150% of the average particle diameter. This is caused by the template encapsulating multiple or coalesced particles, which hinders the ability to detect ghost particles based on its irregular shape.

3.2.2. Selection of an optimal Γ_{th}. As discussed previously in section 2, a histogram-based thresholding technique is used to eliminate voxels, which are considered to be either the background, ghost particles or noise. This requires us to define a threshold (Γ_{th}) that can be used to eliminate ghost particles and noise but will have minimal impact on actual particles present in the reconstructed intensity field. In this section, we analyse the influence that N_s has on the selection of the optimal Γ_{th}. To perform this, simulations are run at several N_s and Γ_{th} levels. It should be noted that a level of $\Gamma_{th} = 0$ corresponds to a control case where SMRE does not modify the reconstructed intensity field. This case is used to quantify any improvement in the flow statistics. Similar to the analysis of T_{sz} in section 3.2.1, all other parameters are kept constant and are summarized in table 1.

Figure 11(*a*) shows the variation in the accuracy between simulation and averaged DNS statistics for the mean streamwise velocity at varying Γ_{th} and N_s. A clear improvement is visible at all N_s considered in comparison to the unmodified reconstructed intensity field where Γ_{th} is equal to 0. For example, at $N_s \approx 0.15$, we see an improvement in the percentage error from 0.25% to 0.20% at $\Gamma_{th} = 0.1$ after the application of SMRE. A large improvement is seen at seeding densities higher than $N_s > 0.25$, which is above what is typically used for Tomo-PIV experiments. Therefore, this enables the use of higher seeding densities in Tomo-PIV experiments than what is typically used currently. Similar results are also observed by Novara *et al* (2010) where large improvements are noted at higher seeding densities after the use of MTE-MART to reduce ghost particles. Furthermore, the results suggest that the optimum threshold is a function of N_s and increases at higher N_s. This is caused by an increase in ghost particles present in the reconstructed intensity field at higher N_s, which requires an increasingly aggressive Γ_{th} to eliminate the ghost particles present. We consider the region encapsulated by the contour line indicating an error of 0.25% (indicated in figure 11(*a*)) in comparison to DNS data as a typical uncertainty associated with mean flow statistics (Tropea *et al* 2007). Therefore, within this region, a best-fit second-order polynomial given by

$$\Gamma_{th} = -2.45N_s^2 + 1.76N_s - 0.13 \tag{5}$$

is used to determine the optimal Γ_{th} at a given N_s. Since figure 11(*b*) shows a similar trend to the accuracy for $\langle k\rangle^+$ in comparison to $\langle U\rangle^+$, we recommend the polynomial determined from $\langle U\rangle^+$ (a first-order statistic) as it is considered to be a more reliable indication of the accuracy.

Figure 12 shows that a $\Gamma_{th} \approx 0.10$ corresponds to a detection rate of approximately 15% of the total voxels within

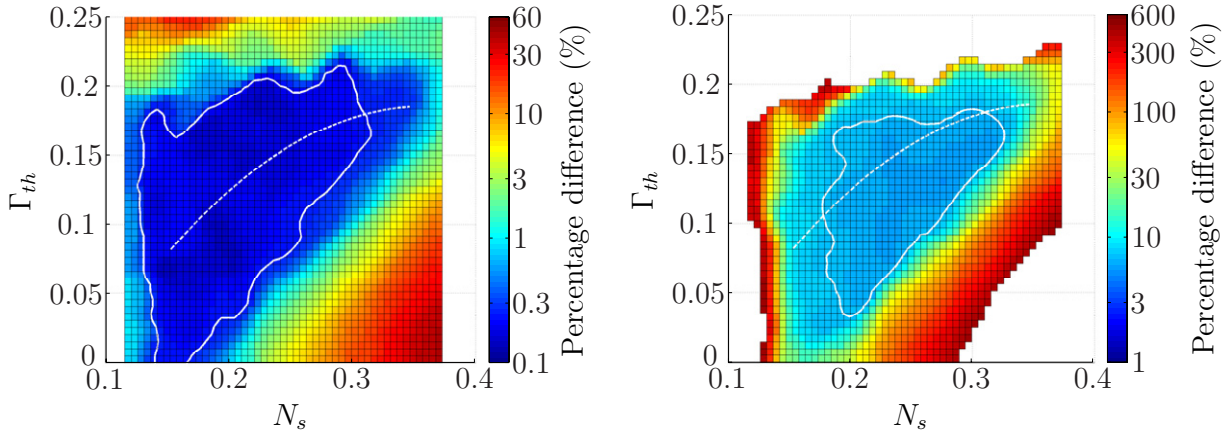

(*a*) Accuracy of $\langle U \rangle^+$. (*b*) Accuracy of $\langle k \rangle^+$.

Figure 11. Comparison of simulation results and averaged DNS statistics for (*a*) $\langle U \rangle^+$ and (*b*) $\langle k \rangle^+$ at varying Γ_{th} and N_s. A Γ_{th} of zero indicates simulations without the use of SMRE. The white solid lines in (*a*) and (*b*) indicate contour levels of 0.25% and 7%, respectively. The optimum threshold polynomial given by equation (5) is shown by the dashed white line.

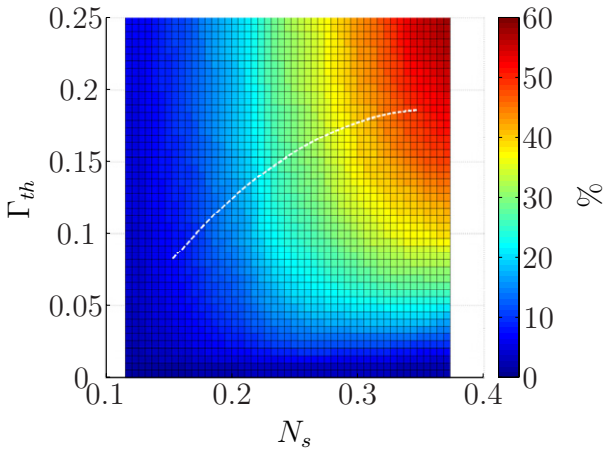

Figure 12. Percentage of voxels detected as ghost particles in the reconstructed intensity field after the application of SMRE at varying N_s and Γ_{th}. The optimum threshold polynomial given by equation (5) is shown by the dashed white line.

the reconstructed intensity field as ghost particles. As N_s is increased the detection rate increases, which is caused by an increase in ghost particles. It should be noted that in contrast to the parameter T_{sz} the optimum Γ_{th} can be influenced by the laser-sheet thickness, since we expect the optimal Γ_{th} to increase as the laser sheet is widened, due to the elevated number of ghost particles. However, as shown in figure 6, the optimal Γ_{th} remains nominally consistent at different laser-sheet thicknesses. In conclusion, a conservative recommendation of $\Gamma_{\text{th}} \approx 0.10$ would provide an improvement in Q for a range of laser-sheet thicknesses, while minimizing the probability of removing actual particles for N_s typically used in Tomo-PIV experiments.

4. Experimental validation

The applicability of SMRE to Tomo-PIV data is verified by the analysis of a data set from a Tomo-PIV experiment. To enable a quantitative analysis on any indicative improvement in the reconstruction quality after the application of SMRE, the experiments are performed at the matched Reynolds number ($Re_\tau = 937$) to the DNS data used in the simulation study. In addition, this allows us to obtain a realistic assessment of the attainable accuracy in a Tomo-PIV experiment for wall-bounded turbulent flows and to report on its limitations for this application. The experiments have been conducted in the Walter Bassett Aerodynamics Laboratory at the University of Melbourne. Details of the construction of the channel flow facility are provided in Monty (2005). Figure 13 shows a schematic of the channel flow facility. The facility is a blower-type tunnel and consists of a dc motor and controller with a fan that is able to generate a volume flow rate of approximately 3.6 $\text{m}^3\ \text{s}^{-1}$, which equates to a bulk velocity of approximately 30 m s^{-1} in the working section. The flow is straightened in a honeycomb section after which it passes through a series of meshes in the diffuser and the settling chamber. This ensures that the flow is uniform with minimal turbulence at the contraction inlet. The flow then enters a two-dimensional contraction (area ratio of 9:1). Experiments conducted by Monty (2005) verified that the flow exiting the contraction is near-uniform with a mean velocity within ±0.5% of the centreline velocity. The channel flow working section consists of nine modular sections constructed using a medium density fibreboard (MDF), supported by side walls constructed using 6 mm thick aluminium C-section. The working section measures 22 m in length with a width and height of 1170 mm and 100 mm, respectively.

The facility includes a modified section to accommodate the Tomo-PIV experimental setup. The modified PIV section consists of a glass floor and walls that span 1400 mm in the streamwise direction. The roof consists of a removable glass section enabling internal access for the PIV calibration procedure, which requires the placement of a calibration target in the region of interest. Figure 14 shows a schematic of the Tomo-PIV experimental setup used in this analysis. The tomographic imaging system consists of four PCO4000

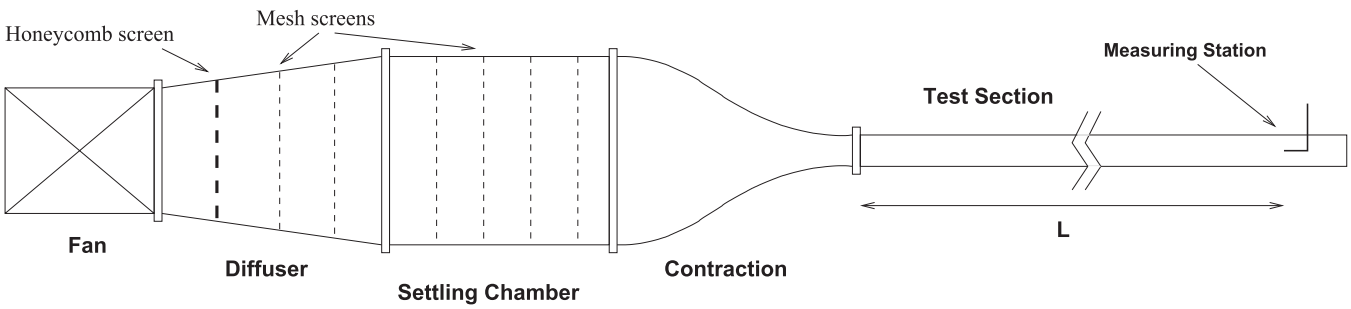

Figure 13. Schematic diagram of channel flow facility at the University of Melbourne (Monty 2005).

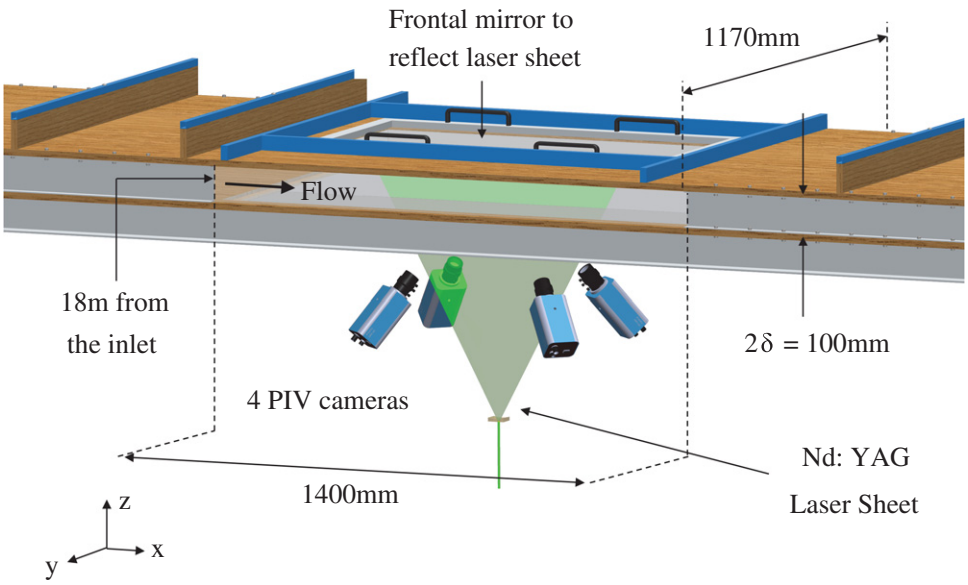

Figure 14. Experimental setup for Tomo-PIV in channel flow.

cameras (4008 × 2672 pixels, 2 Hz) equipped with 105 mm Nikon lenses. The above setup enables us to obtain a reconstructed volume size of $\approx 1.5\delta \times 1\delta \times 0.2\delta$, where δ denotes the half-channel height. The cameras are positioned and orientated to within $\pm 5^\circ$ of the optimum azimuthal ($\theta \approx 23^\circ$) and elevation ($\phi \approx 55^\circ$) angles as specified by de Silva *et al* (2012). A frontal mirror is used to reflect the laser light to improve illumination for the given camera configuration. The flow is seeded with polyamide particles with a mean particle diameter of 1 μm with a seeding density of $N_s \approx 0.15$. The particles are illuminated using a dual cavity Big Sky Nd:YAG laser.

The experimental data are processed using an in-house Tomo-PIV package; details of the algorithms used for reconstruction and cross-correlation are given in de Silva *et al* (2012). A pixel to voxel ratio of 1 is maintained in the reconstruction, giving a volume size of 4008 × 2672 × 534 voxels. In addition, the cross-correlation is performed with an interrogation volume length of $l^+ \approx 10$ with a corresponding voxel characteristic length of $l_v^+ \approx 0.41$. The parameters Γ_{th} and T_{sz} are chosen to match the optimal values for the given experimental conditions as suggested in sections 3.2.1 and 3.2.2.

The verification of SMRE is performed by comparing DNS and experimental Tomo-PIV flow statistics. To enable this, an image set with a thousand frames is captured to obtain first- and second-order statistics which are verified for convergence. These experimental flow statistics are then compared to the original DNS statistics (del Alamo *et al* 2004) and DNS statistics averaged over the same interrogation volume length used in the experiment (averaged DNS statistics). Here, we use several DNS fields to obtain converged DNS and averaged DNS statistics. The three-dimensional box-filter size of the averaged DNS statistics is matched with the interrogation volume size; therefore, a comparison between the experimental and the averaged DNS statistics provides a quantitative assessment of the accuracy associated with the Tomo-PIV technique in wall-bounded turbulent flows. To reduce the processing time, a quantitative comparison is performed in the region $400 < z^+ < 550$.

Table 2 summarizes the accuracy of first- and second-order flow statistics between the experimental, DNS and averaged DNS data before and after the application of SMRE. The results suggest an improvement in accuracy of all the flow statistics considered after the application of SMRE. This is particularly evident in the second-order statistics where an improvement of over 15% is observed in certain cases. In addition, we observe a reduction of approximately 20% in spurious vectors based on the detection criteria suggested by Westerweel and Scarano (2005). A comparison

Table 2. Summary of absolute percentage errors for flow statistics in the region $400 < z^+ < 550$ with an interrogation volume length of $l^+ = 10$.

	Conventional reconstruction	Modified reconstruction
Experimental Tomo-PIV versus DNS statistics		
$\langle U \rangle^+$	0.14%	0.12%
$\langle u^2 \rangle^+$	3.19%	2.71%
$\langle v^2 \rangle^+$	7.19%	5.61%
$\langle w^2 \rangle^+$	12.63%	10.70%
Experimental Tomo-PIV versus averaged DNS statistics		
$\langle U \rangle^+$	0.14%	0.12%
$\langle u^2 \rangle^+$	2.18%	1.70%
$\langle v^2 \rangle^+$	5.50%	3.80%
$\langle w^2 \rangle^+$	10.72%	8.75%

to the simulation results presented previously with similar experimental parameters indicates that the simulations provide a good estimate of the achievable accuracy. As expected, the experimental results show a higher error. This is primarily because the simulations are idealistic in comparison to an actual experiment, which is affected by fixed pattern noise, lens aberrations, foreign objects, reflections and calibration errors.

5. Conclusion

A new scheme (simulacrum matching-based reconstruction enhancement) to reduce ghost particles in a reconstructed intensity field for Tomo-PIV has been developed. Results indicate that the removal of ghost particles causes a substantial improvement in the quality of the vector fields obtained from Tomo-PIV measurements. An analysis is performed on the key parameters of SMRE, which include the threshold (Γ_{th}) which is used by SMRE in a histogram-based thresholding technique to distinguish ghost particles. Results suggest that the optimum Γ_{th} varies with seeding density (N_s) and can be determined using equation (5) for a given N_s. It is observed that a value of $\Gamma_{\text{th}} = 0.10$ works well for the range of N_s typically used in Tomo-PIV experiments. In addition, we also conclude that the optimum template size (T_{sz}) is proportional to the mean particle diameter and should be 1–2 voxels larger than the mean particle diameter.

An assessment of the quality factor Q showed an improvement in reconstruction quality with the application of SMRE at various N_s. An improvement greater than 20% in Q is achieved in the range $0.17 < N_s < 0.35$. Furthermore, the range of N_s where an acceptable accuracy of first- and second-order flow statistics is obtained after using SMRE is twice as large as those currently reported in the literature for Tomo-PIV experiments. Similar results are also observed by Novara *et al* (2010) after the application of MTE-MART to reduce ghost particles where high seeding densities are improved considerably. We can conclude from the simulations that the impact on actual particles is minimal and SMRE is sufficiently robust to accommodate larger coalesced particles as discussed earlier. This is illustrated in figures 5(*a*) and (*b*).

The application of SMRE to real experimental data obtained from a Tomo-PIV experiment shows that an improvement of up to 15% is obtained for second-order flow statistics. In addition, a 20% reduction in spurious vectors is observed similar to the improvement indicated in the simulation study. These results indicate an improvement in Q and thereby a reduction in measurement uncertainties, and an improved representation of the measured velocity field. It should be noted that SMRE can be applied to many applications of Tomo-PIV experiments independent of the reconstruction algorithm.

Acknowledgments

The authors gratefully thank Professor R D Moser for making the $Re_\tau = 934$, DNS data available, and the financial support of the Australian Research Council.

References

Adrian R J 2005 Twenty years of particle image velocimetry *Exp. Fluids* **39** 159–69

Adrian R J and Westerweel J 2011 *Particle Image Velocimetry* (Cambridge: Cambridge University Press)

Atkinson C, Coudert S, Foucaut J M, Stanislas M and Soria J 2011 The accuracy of tomographic particle image velocimetry for measurements of a turbulent boundary layer *Exp. Fluids* **50** 1031–56

Atkinson C and Soria J 2009 An efficient simultaneous reconstruction technique for tomographic particle image velocimetry *Exp. Fluids* **47** 553–68

Barnhart D H, Adrian R J and Papen G C 1994 Phase-conjugate holographic system for high-resolution particle-image velocimetry *Appl. Opt.* **33** 7159–70

Belden J, Truscott T T, Axiak M C and Techet A H 2010 Three-dimensional synthetic aperture particle image velocimetry *Meas. Sci. Technol.* **21** 125403

Brücker C 1996 3D scanning-particle-image-velocimetry: technique and application to a spherical cap wake flow *Appl. Sci. Res.* **56** 157–79

de Silva C M, Baidya R, Khashehchi M and Marusic I 2012 Assessment of tomographic PIV in wall-bounded turbulence using direct numerical simulation data *Exp. Fluids* **52** 425–40

del Alamo J C, Jimenez J, Zandonade P and Moser R D 2004 Scaling of the energy spectra of turbulent channels *J. Fluid Mech.* **500** 135–44

Elsinga G E, Scarano F, Wieneke B and van Oudheusden B W 2006 Tomographic particle image velocimetry *Exp. Fluids* **41** 933–47

Keane R D and Adrian R J 1992 Theory of cross-correlation of PIV images *Appl. Sci. Res.* **49** 191–215

Lecordier B and Westerweel J 2008 The EUROPIV synthetic image generator *Technical Report*

Lewis J P 1995 Fast normalized cross-correlation *Int. Conf. Vision Interface*

Maas H, Gruen A and Papantoniou D 1993 Particle tracking velocimetry in three-dimensional flows *Exp. Fluids* **15** 133–46

Monty J P 2005 Developments in smooth wall turbulent duct flows *PhD Thesis* The University of Melbourne, Victoria, Australia

Novara M, Batenburg K J and Scarano F 2010 Motion tracking-enhanced MART for tomographic PIV *Meas. Sci. Technol.* **21** 035401

Phong B T 1975 Illumination for computer generated pictures *Commun. ACM* **18** 311–7
Scarano F 2001 Iterative image deformation methods in PIV *Meas. Sci. Technol.* **13** R1–19
Scarano F, Elsinga G E, Bocci E and van Oudheusden B W 2006 Investigation of 3D coherent structures in the turbulent cylinder wake using Tomo-PIV *13th Int. Symp. on Applications of Laser Techniques to Fluid Mechanics*
Scarano F and Poelma C 2009 Three-dimensional vorticity patterns of cylinder wakes *Exp. Fluids* **47** 69
Schröder A, Geisler R, Elsinga G E, Scarano F and Dierksheide U 2008 Investigation of a turbulent spot and a tripped turbulent boundary layer flow using time-resolved tomographic PIV *Exp. Fluids* **44** 305–15
Tropea C, Yarin L A and Foss J F 2007 *Springer Handbook of Experimental Fluid Mechanics* (Heidelberg: Springer)
Westerweel J and Scarano F 2005 Universal outlier detection for PIV data *Exp. Fluids* **39** 1096–100
Willert C E and Gharib C E 1992 Three-dimensional particle imaging with a single camera *Exp. Fluids* **12** 353–8
Worth N A and Nickels T B 2008 Acceleration of Tomo-PIV by estimating the initial volume intensity distribution *Exp. Fluids* **45** 847–56